INORGANIC CHEMISTRY FRONTIERS

RESEARCH ARTICLE

View Article Online
View Journal

Cite this: DOI: 10.1039/d5qi01111f

Charge transfer stimulated visible-light photochromism of naphthalenediimide-based zinc halide coordination polymers for detecting/filtering harmful blue rays†

Xiaojuan Zhang,[a] Ming Kang,[a] Shimin Zhang,[b] Jingfang Wang,[a] Yifang Zhang,[a] Pengfei Hao, *[a] Junju Shen *[a] and Yunlong Fu *[a]

Received 9th May 2025,
Accepted 19th June 2025

DOI: 10.1039/d5qi01111f

rsc.li/frontiers-inorganic

Due to high penetration, low photo-toxicity, and low background signal of red-shifted visible light, the development of visible-light photochromic materials is of great importance but still a challenging task. In this study, four one-dimensional (1D) naphthalenediimide (NDI) photochromic coordination polymers (CPs), namely $\{[ZnCl_2(4\text{-PMNDI})]\cdot H_2O\}_n$ (**1**), $\{[ZnBr_2(4\text{-PMNDI})]\cdot 2H_2O\}_n$ (**2**), $\{[ZnCl_2(3\text{-PMNDI})]\}_n$ (**3**) and $\{[ZnBr_2(3\text{-PMNDI})]\}_n$ (**4**) (4-/3-PMNDI = *N*,*N*′-bis(4-/3-pyridylmethyl)-1,4,5,8-naphthalenediimide), have been designed and synthesized by the combination of positional isomeric electron-deficient PMNDI (electron acceptors, EAs) and electron-rich zinc halides (electron donors, EDs) under solvothermal conditions. The distinct photochromic properties of **1–4** should be attributed to the formation of different interfacial contacts of EDs/EAs due to the introduction of 4-/3-PMNDI positional isomers and different halogen anions. Noteworthily, the much more rapid photoresponsive rates of visible-light photochromism for **1–4** with respect to those of UV-light photochromism exposits that the electronic absorption band of charge transfer (CT) interactions in the visible light region can effectively trigger electron transfer (ET) promptly. Furthermore, **1** exhibits a high photosensitivity property in response to wavelengths of 390–450 nm, and it can be applied in detection/filtration of harmful blue rays. This work breaks through an orthodox concept that the ET reaction can only be activated by the electronic absorption band of EDs or EAs (usually in the UV light region), and provides a simple and feasible method for the construction of visible-light photochromic materials.

Introduction

Visible light photochromic materials, as a new class of functional materials, have attracted wide attention due to their practical and potential applications in the fields of materials science, optoelectronics and biomedicine.[1–4] So far, visible-light photochromic organic molecules based on the mechanism of photoisomerization, such as diarylethenes,[5,6] azobenzenes,[7,8] spiropyrans,[9,10] and Stenhouse adducts,[11,12] have been extensively investigated. However, the relatively low photosensitivity and photoisomerization efficiency highly restrict the actual applications of such visible-light photochromic materials. Therefore, the development of novel visible-light photochromic materials does not depend on photoisomerization but depends on photoinduced intermolecular electron transfer (PIET), which should be an effective strategy for addressing the above disadvantages of visible-light photochromic organic molecules.

Notably, organic–inorganic hybrid photochromic systems (OIHPS) composed of electron donors (EDs) and electron acceptors (EAs) possess a large number of advantages (flexible and diverse compositions and structures, easy molecular design and synergistic effect), which provide a tremendous opportunity for the development of visible-light induced photochromic materials.[13–17] By the selection and integration of suitable EDs/EAs, great achievements have been achieved in terms of fast photoresponsive rates, obvious coloration contrast, wide photoresponsive range and so forth. Unfortunately, the activation wavelengths of most reported OIHPS on the basis of PIET are usually located in the UV region, which is

[a]*Key Laboratory of Magnetic Molecules & Magnetic Information Materials Ministry of Education, School of Chemical and Material Science, Shanxi Normal University, Taiyuan 030031, China. E-mail: haopengfei_2015@126.com, shenjj@sxnu.edu.cn, yunlongfu@sxnu.edu.cn*

[b]*Department of Applied Chemistry, Yuncheng University, Yuncheng 044000, China*

†Electronic supplementary information (ESI) available: PXRD patterns, TGA curves, IR spectra, EPR spectra, XPS spectra, crystal data and structure refinement, selected bond lengths and angles, and hydrogen bonds. CCDC 2412670–2412672. For ESI and crystallographic data in CIF or other electronic format see DOI: https://doi.org/10.1039/d5qi01111f

largely ascribed to the excitation mechanism of OIHPS. PIET refers to the generation of a charge-separated state induced by light irradiation, in which electrons transfer from an electron donor (ED) to an electron acceptor (EA). Up to now, the pathway of the photoexcitation mechanism can be classified into two different categories, the photoexcitation of an EA or an ED.[18–20] As for the former, the photoexcited state EA* is formed and it can accept electrons from the HOMO of the ED to generate organic radicals ($ED^{\bullet+}$ and $EA^{\bullet-}$) (Fig. 1a), which necessitates high-energy UV light illumination, because the electronic absorption band of EAs (the unsaturated organic electron-deficient acceptors, such as viologen derivatives,[21,22] naphthalenediimide derivatives (NDIs)[23,24] and tris(4-pyridyl)-1,3,5-triazine (TPT))[25,26] is usually located in the UV region. As for the latter, the photoexcited state ED* is generated which then transfers electrons to the LUMO of the EA to form the same organic radicals ($ED^{\bullet+}$ and $EA^{\bullet-}$) (Fig. 1b) as the former, which can be stimulated by the low-energy visible light band through the selection of an ED (visible light photosensitizers such as cadmium sulfide,[27] polyoxometalates[28–30] and inorganic semiconductors[31]) with a low optical bandgap and high light absorption coefficient. However, the reported OIHPS based on the photoexcitation of the ED are extremely scarce, which significantly restricts the diversity and practical application of visible-light responsive functional materials. Therefore, developing a novel visible light photoexcitation mechanism will facilitate the construction of a new category of visible-light responsive OIHPS and the development of the emerging field. The strength of charge transfer (CT) interaction is dependent on the degree of orbital overlap of the ED/EA, and it determines the non-characteristic electronic absorption band of the OIHPS, which is generally situated in the visible-light region. In our previous study, we found that charge transfer (CT) could extend the excitonic absorption to the visible-light region and enable the fabrication of a super excellent visible-light photochromic system.[32–34] As a result, elaborate modulation of the electronic absorption band of CT interaction is applied to stimulate ET from the HOMO of an ED to the LUMO of an EA and consequently generate the organic radicals $ED^{\bullet+}$ and $EA^{\bullet-}$ (Fig. 1c), which will be an effective strategy for the construction of novel visible-light responsive OIHPS.

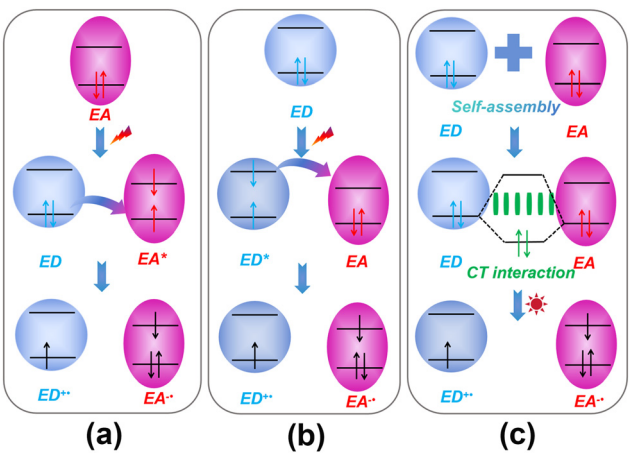

Fig. 1 Schematic diagram of photoinduced intermolecular electron transfer: (a) The excitation of electron acceptor (EA). (b) The excitation of electron donor (ED). (c) The excitation of charge transfer (CT) electronic absorption band.

NDIs are a class of outstanding electron-deficient organic tectons with high redox activity and have been extensively applied in the fabrication of stimuli-responsive functional materials, with properties such as photochromism, thermochromism and electrochromism.[35–38] On the one hand, the modification on both sides of the NDI nucleus by using pyridylmethylene groups could not only merely regulate their electron-accepting capability to some degree, but also endow them with flexible property to modulate the formation of specific interfacial contacts of EDs/EAs and consequently generate the electronic absorption band in the visible light region. On the other hand, the electron-deficient NDI moiety is inclined to form various degrees of CT interactions through weak interactions (such as lone pair–π, anion–π and π–π interactions) with an electron-rich moiety, making it an outstanding candidate for fabrication of visible-light responsive OIHPS.

Based on the above consideration, the combination of a couple of positional isomers (4-/3-PMNDI) and electron-rich zinc halides ($ZnCl_2$ and $ZnBr_2$) gives rise to four one-dimensional (1D) naphthalenediimide (NDI) coordination polymers (CPs), $\{[ZnCl_2(4\text{-PMNDI})]\cdot H_2O\}_n$ (**1**), $\{[ZnBr_2(4\text{-PMNDI})]\cdot 2H_2O\}_n$ (**2**), $\{[ZnCl_2(3\text{-PMNDI})]\}_n$ (**3**) and $\{[ZnBr_2(3\text{-PMNDI})]\}_n$ (**4**). Here, 4-/3-PMNDI = *N*,*N*′-bis(4-/3-pyridylmethyl)-1,4,5,8-naphthalenediimide, which exhibit different photochromic performances in response to UV and visible light owing to the formation of different interfacial contacts of EDs/EAs. Interestingly, the photoresponsive rates of visible-light photochromism for **1–4** are much faster than those of UV-light photochromism, which reveals that the electronic absorption bands of the CT interactions in the visible light region can efficiently induce ET quickly. Fascinatingly, **1** is extremely sensitive to harmful blue rays ranging from 390 to 450 nm and can accurately detect/filter harmful blue rays. This work not only develops a novel photoexcitation mechanism for initiating the ET reaction to construct visible-light photochromic materials, but also provides a simple and effective pathway for detecting/filtering harmful blue rays.

Experimental section

Materials and methods

All reagents and solvents of reagent grade were purchased from commercial sources and used without further purification. The organic ligands 4-/3-PMNDI were prepared using the reported process[39] (Scheme S1†). A mercury (Hg) lamp (300 W, 365 nm) system equipped with a temperature controller and a xenon (Xe) lamp (300 W, >420 nm) system with a temperature controller and a UV filter were applied for prepar-

ing colored samples for UV-vis absorption spectroscopy, in which the distances between these samples and the Hg/Xe lamp were about 23 cm. UV-vis absorption spectra were measured with a METASH UV-9000S UV-vis spectrophotometer equipped with an integrating sphere, and a $BaSO_4$-coated glass slide as a reference at room temperature. Thermogravimetric analysis-differential scanning calorimetry (TG-DSC) data were obtained in a nitrogen atmosphere with a flow rate of 100 cm^3 min^{-1}, thermal ramp of 10 °C min^{-1}, and temperature range of 30–800 °C using an HCT-2 thermogravimetric analyzer. The Fourier transform infrared (FT-IR) spectra were recorded in the range of 4000–500 cm^{-1} on a Nicolet 5DX spectrometer using KBr pellets as the matrixes. Powder X-ray diffraction (PXRD) patterns were acquired using a Rigaku UItima IV-185 diffractometer with 2θ ranging from 5° to 50° at room temperature. The simulated PXRD patterns were derived using the free Mercury software based on the single-crystal data. Elemental analyses (C, H, N) were executed on a PerkinElmer 240 elemental analyzer. Electron paramagnetic resonance (EPR) spectra were recorded on a Bruker A300-10/12 electron paramagnetic resonance spectrometer at ambient temperature. X-ray photoelectron spectroscopy (XPS) measurements were conducted on a Kratos AXIS ULTRA X-ray photoelectron spectrometer with Al Kα radiation (λ = 8.357 Å). All XPS spectra were referenced to the C 1s neutral carbon peak at 284.8 eV in order to compensate for surface charging effects. Luminescence properties were measured using an HORIBA Instruments FluoroMAX Plus fluorescence spectrometer.

Preparation of $\{[ZnCl_2(4\text{-PMNDI})]\cdot H_2O\}_n$ (1)

A mixture of 4-PMNDI (0.013 g, 0.03 mmol) and $ZnCl_2$ (0.008 g, 0.06 mmol) in a solution (5 mL) of DMF/MeCN (3 : 2, v/v) was stirred for 10 minutes. Then, the mixture was sealed in a 25 mL Teflon reactor autoclave and heated at 80 °C for 4 days (Scheme S2†). After cooling down to room temperature, the products were collected, further washed with DMF and finally dried in the air at room temperature to obtain light yellow plate crystals with a yield of 47% (based on 4-PMNDI). Anal. calcd for $C_{26}H_{18}Cl_2N_4O_5Zn$ (%): C, 51.81; H, 3.01; N, 9.30. Found: C, 51.63; H, 3.05; N, 9.36. IR data (KBr, cm^{-1}): 3477(s), 3050(w), 1704(s), 1658(s), 1617(m), 1587(m), 1558(w), 1502(w), 1454(m), 1428(s), 1337(w), 1255(m), 1218(w), 1180(s), 1120(m), 1095(w), 1066(w), 1029(w), 1004(s), 889(w), 869(w), 809(m), 779(m), 717(s), 644(s), 563(m).

Preparation of $\{[ZnBr_2(4\text{-PMNDI})]\cdot 2H_2O\}_n$ (2)

The procedure was analogous to the synthesis of compound **1** except that the $ZnCl_2$ was replaced with $ZnBr_2$ (0.02 g, 0.09 mmol) and the reaction temperature was maintained at 95 °C for 2 days. Yellow plate crystals were isolated in a yield of 52% (based on 4-PMNDI). Anal. calcd for $C_{26}H_{20}Br_2N_4O_6Zn$ (%): C, 44.01; H, 2.84; N, 7.90. Found: C, 44.05; H, 2.81; N, 7.95. IR data (KBr, cm^{-1}): 3488(s), 3046(s), 1706(s), 1668(s), 1619(s), 1587(m), 1558(w), 1502(w), 1454(m), 1428(s), 1373(w), 1338(w), 1249(m), 1180(s), 1120(m), 1095(w), 1068(w), 1029(w), 997(s), 889(w), 869(w), 806(m), 769(m), 717(w), 640(m), 561(m).

Preparation of $\{[ZnCl_2(3\text{-PMNDI})]\}_n$ (3)

The procedure was analogous to the synthesis of compound **1**, except that the 4-PMNDI was replaced with 3-PMNDI. Light brown plate crystals of **3** were obtained in 52.0% yield (based on 3-PMNDI). Anal. calcd for $C_{26}H_{16}Cl_2N_4O_4Zn$ (%): C, 53.40; H, 2.76; N, 9.58. Found: C, 53.20; H, 2.51; N, 9.63. IR data (KBr, cm^{-1}): 3471(w), 3056(w), 2022(w), 1706(s), 1695(s), 1608(s), 1569(m), 1515(w), 1455(s), 1420(s), 1373(s), 1332(w), 1240(m), 1205(w), 1162(m), 1150(m), 1132(s), 1095(w), 1056(m), 977(m), 898(m), 846(m), 794(s), 761(s), 682(m), 647(m), 538(m).

Preparation of $\{[ZnBr_2(3\text{-PMNDI})]\}_n$ (4)

The procedure was analogous to the synthesis of compound **2**, except that the 4-PMNDI was replaced with 3-PMNDI. Light brown plate crystals of **4** were obtained in 49% yield (based on 3-PMNDI). Anal. calcd for $C_{26}H_{16}Br_2N_4O_4Zn$ (%): C, 46.35; H, 2.39; N, 8.32. Found: C, 46.38; H, 2.35; N, 8.44. IR data (KBr, cm^{-1}): 3469(s), 2923(s), 1693(s), 1668(w), 1660(s), 1577(s), 1482(m), 1448(m), 1371(w), 1320(m), 1249(m), 1205(w), 1172(m), 1128(w), 1091(s), 1064(w), 1000(s), 971(w), 896(m), 848(w), 771(w), 792(w), 692(m), 649(m), 561(m).

Single crystal X-ray structure determination and refinement

The diffraction data were collected on a Bruker D8 Venture diffractometer equipped with a graphite monochromator (Mo Kα, λ = 0.71073 Å) at 293 K for **2–4**. The SCALE3 ABSPACK scaling algorithm utilized empirical absorption correction with spherical harmonics. All structures were solved by direct methods and refined based on F^2 by the full matrix least-squares method with the Olex2 software.[40,41] All non-hydrogen atoms were refined using anisotropic thermal parameters, and all hydrogen atoms were calculated and added at the theoretical positions. Relevant crystallographic data, selected bond lengths, bond angles and hydrogen-bond parameters are summarized in Tables S3–S5 of the ESI.†

Results and discussion

Crystal structures of 1 and 2

Single-crystal X-ray diffraction analyses revealed that **1** and **2** are isostructural and crystallize in the monoclinic system with the space group *C*2/*c*, which contains one half crystallographically independent Zn^{2+} ion, one halogen anion (X = Cl for **1** and Br for **2**), one half 4-PMNDI ligand, and one half free H_2O molecule for **1** and one for **2** in the asymmetric unit. Since the crystal structure of **1** is reported in the literature,[42] herein the details of the structure are not described. As shown in Fig. 2a, each central Zn^{2+} ion is coordinated in tetrahedral sites by two terminal bromine atoms (d_{Zn-Br} = 2.337(8) Å) and two nitrogen atoms from two 4-PMNDI ligands (d_{Zn-N} = 2.062(5) Å). The Br–Zn–Br angle is 119.27(6)°, the Br–Zn–N angles are in the range of 106.59(1)–111.94(1)°, and the N–Zn–N angle is 98.40(3)° for **2**. According to the descriptor for the deviation of tetrahedral geometry proposed by Yang and coworkers,[43] the τ_4 values of **1**

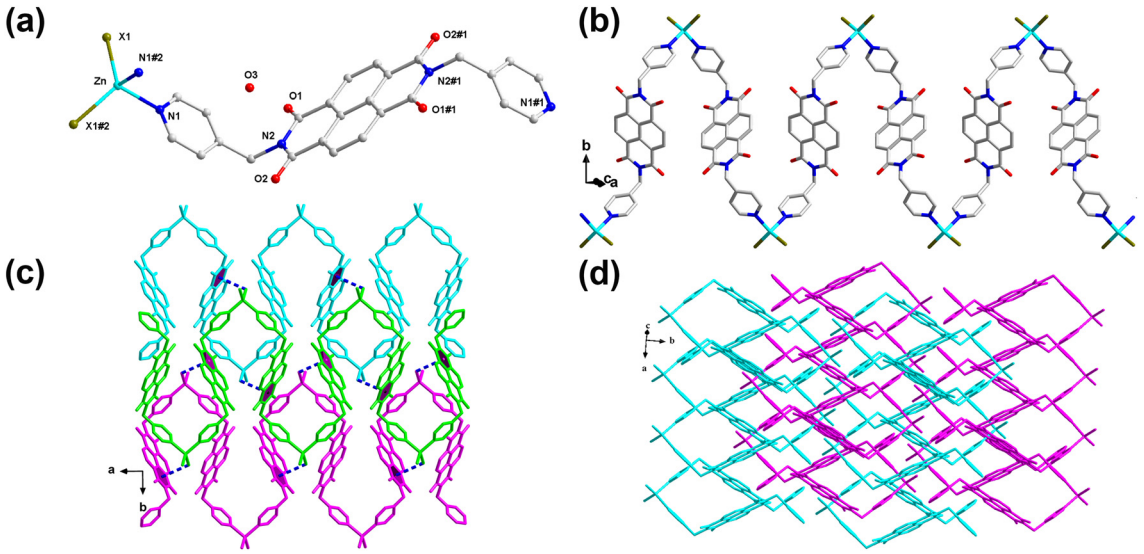

Fig. 2 (a) The coordination environment of Zn^{2+} in **1** and **2** (symmetry codes: #1: $-x, +y, \frac{1}{2}-z$; #2: $\frac{1}{2}-x, 3/2-y, 1-z$). (b) The 1D infinite chain. (c) The anion–π interactions in adjacent chains. (d) The 3D packing supramolecular network. All hydrogen atoms are omitted for clarity.

and **2** are 0.909 and 0.913, respectively, implying a slightly distorted ZnN_2Cl_2 tetrahedron compared to that of the ZnN_2Br_2 tetrahedron. The dihedral angle between the 4-PMNDI core and the pyridine ring plane is 69.656°, which is similar to that previously reported for the free 4-PMNDI ligand.[44] Zn^{2+} ions are connected by 4-PMNDI ligands with a *Z*-mode conformation, forming a one-dimensional (1D) V-shaped polymeric chain (Fig. 2b). The single chain undergoes translation along the *b* direction (Fig. 2c), which interleaves it with adjacent four chains through anion–π interactions between NDI cores and halogen atoms ($d_{Cl\text{-}\pi}$ = 3.319(4) Å for **1** and $d_{Br\text{-}\pi}$ = 3.332(8) for **2**) to form a three-dimensional (3D) supramolecular network (Fig. 2d).

Crystal structures of 3 and 4

Compounds **3** and **4** are isostructural and crystallize in the monoclinic system with the space group *C*2/*c*, which contains one half crystallographically independent Zn^{2+} ion, one half 3-PMNDI ligand and one halogen anion (X = Cl for **3** and Br for **4**) in the asymmetric unit. As depicted in Fig. 3a, each central Zn^{2+} ion is four-coordinated with two terminal X atoms (Cl in **3** and Br in **4**) and two N atoms from two electron-deficient 3-PMNDI tectons. The Zn–X bond length is 2.223(6) Å for **3** and 2.358(3) Å for **4**, and the Zn–N bond distance is 2.069 (2) Å for **3** and 2.071(2) Å for **4**, which are well in accordance with those found in other zinc based coordination polymers.[45] The X–Zn–X angle is 128.69(4)° for **3** and 126.06(2)° for **4**, and the N–Zn–N angle is 103.62(1)° for **3** and 104.35(1)° for **4**. The calculated τ_4 values of **3** (0.877) and **4** (0.894) are slightly smaller than those of **1** and **2**, while the dihedral angles between the NDI core and the pyridine ring plane of **3** (113.11 Å) and **4** (111.96 Å) are much larger than those for **1** and **2**. These differences in structural parameters are largely ascribed to the use of positional isomers of 4-/3-PMNDI. Zinc ions are bridged by the 3-PMNDI ligand in a *Z*-mode conformation to form a nearly straight zigzag shaped chain (Fig. 3b). Each chains are further connected with each other by lone pair–π weak interactions ($d_{o\text{-}\pi}$ = 3.606(3) Å in **3** and $d_{o\text{-}\pi}$ = 3.719 (3) Å in **4**) and π–π interactions ($d_{\pi\text{-}\pi}$ = 3.822(3) Å in **3** and $d_{\pi\text{-}\pi}$ = 3.929(3) Å in **4**) (Fig. 3c), to form a two dimensional (2D) supramolecular layer (Fig. 3d).

Thermogravimetric analyses (TGA)

The thermal stability of compounds **1–4** was investigated through thermogravimetric and differential scanning calorimetry (TG-DSC) studies under a nitrogen atmosphere in the temperature range of 30–800 °C (Fig. S1†). TG-DSC curves of **1** and **2** exhibit a two-step decomposition loss and **1** can be stable until 105 °C and **2** up to 383 °C. The first weight loss in the temperature range of 105–155 °C for **1** and 383–391 °C for **2** is around 3.0% and 5.7%, respectively, which is due to the escape of lattice H_2O molecules (calcd: 2.7% for **1** and 4.6% for **2**). Further heating to 451 °C for **1** and 448 °C for **2** causes the decomposition of frameworks. Comparatively, TG-DSC curves of **3** and **4** display one-step weight loss. There is no apparent weight loss before 436 °C for **3** and 412 °C for **4**, and further heating leads to weight loss due to the collapse of frameworks. The different decomposition temperatures of **1–4** are attributed to the use of different halogens and positional isomers of the PMNDI ligands and consequently the formation of different types and strengths of intermolecular interactions.

UV/visible light photochromic properties

The UV-vis absorption spectra of NDIs in a highly dispersed state are usually located in the UV-light region (340–390 nm) as reported by Saha and colleagues.[46,47] However, NDIs in the crystalline state and NDI-based coordination polymers show a redshift with an obvious absorption band in the visible-light

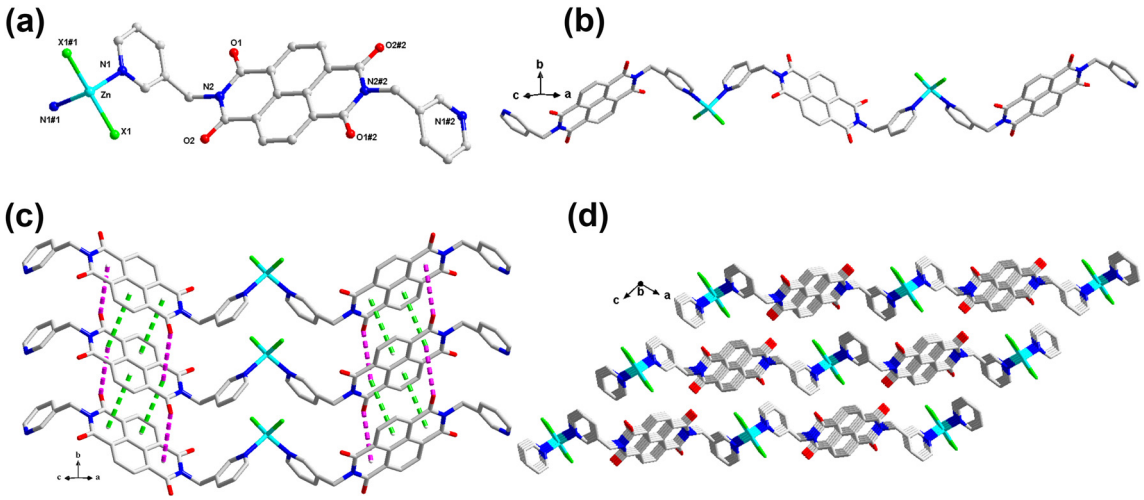

Fig. 3 (a) The coordination environment of Zn^{2+} in **3** and **4** (symmetry codes: #1: $-x, y, \frac{1}{2} - z$, #2: $\frac{1}{2} - x, 5/2 - y, -z$). (b) The 1D polymeric infinite chain. (c) The lone pair–π and π–π interactions. (d) The packing diagram. All hydrogen atoms are omitted for clarity.

region due to the specific arrangements of spatial packing modes at the molecular level through weak interactions (*e.g.* π–π, lone pair–π and anion–π interactions).[48] Similarly, the original absorption bands of **1–4** are located in the visible-light region (390–459 nm for **1**, 390–469 nm for **2**, 390–468 nm for **3** and 390–477 nm for **4**) (Fig. S2†), which are basically consistent with the initial colors of **1–4** (light yellow for **1**, yellow for **2**, and light brown for both **3** and **4**). The obvious red-shifted absorption edges of **3** and **4** compared to those of **1** and **2** should be ascribed to the use of positional isomers of 4-/3-PMNDI which consequently leads to completely different types of weak interactions in the interfacial contacts of EDs/EAs (anion–π interactions for **1** and **2** *vs.* lone pair–π and π–π interactions for **3** and **4**), suggesting the subtle modulating effect of the positionally isomeric PMNDI ligands on intermolecular charge transfer (ICT). Furthermore, the absorption edges of **2** are slightly red-shifted with respect to those of **1**, which is attributed to the occurrence of different strengths of anion–π interactions between the halogen ions (Cl^- ion and Br^- ion) and 4-PMNDI ligands. Although the lone pair–π and π–π interactions in **3** are slightly shorter than those in **4**, the slightly blue-shifted absorption edges of **3** relative to those of **4** are largely ascribed to the use of different halogen ions. These interesting phenomena indicate the delicate modulating effect of halogens on ICT.

Compounds **1–4** are highly photosensitive and show obvious color transformations in response to both UV and visible light. Upon irradiation with a Hg lamp (300 W, 365 nm) at room temperature in air, **1** and **2** change from their initial colors to brownish-black (denoted as **1P-UV**) and dark brown (denoted as **2P-UV**) within 1s (light irradiation 1 s: ΔAbs = 0.11 for **1** and 0.14 for **2**) and the coloration processes are completed within 15 min and 10 min, respectively, while **3** and **4** turn from light brown to brown (denoted as **3P-UV** and **4P-UV**) within 6 s and 60 s (ΔAbs = 0.15 for **3** and **4** upon UV light irradiation of 6 and 60 s, respectively) and reach saturation in 25 min. The positions and intensities of the main peaks in PXRD patterns (Fig. S3†) for **1P-UV–4P-UV** are basically in accordance with those of the fresh samples, ruling out the possibility of photoisomerization and/or photolysis, which is further confirmed by the consistent FT-IR spectra before and after light irradiation (Fig. S4†). In order to elucidate the photochromic mechanism, the time-dependent UV-vis absorption spectra of **1–4** at room temperature were carefully studied and analyzed (Fig. 4 and 5). As shown in Fig. 4, three absorption peaks centred at 483, 608, 757 nm for **1** and 486, 610, 759 nm for **2** are observed in the time-dependent UV-vis absorption spectra, while four peaks at 485, 615, 684, and 760 nm for **3** and 482, 610, 678 and 756 nm for **4** are detected. Although these absorption peaks should be attributed to the characteristic absorption of the colored anion radicals $[NDI]^{\bullet-}$, the different quantity of absorption peaks should be probably due to the use of the positional isomers of 4-/3-PMNDI. With the extension of radiation time, the intensities of these absorption peaks for **1** and **2** dramatically enhance, but those for **3** and **4** gradually increase, in which the amount of $[NDI]^{\bullet-}$ radical anions eventually reach saturation, corresponding to the apparently distinct colored states (brownish black for **1**, dark brown for **2**, and brown for **3** and **4**). Moreover, **1P-UV–4P-UV** could be restored to their initial colors after being left in a dark environment at room temperature for about 12, 12, 7 and 5 days, respectively, indicating the photochromic reversibility of compounds **1–4**. Meanwhile, the decolorization processes of **3** and **4** could also be attained by heat treatment at 140 °C (7 h for **3P-UV** and 4 h for **4P-UV**).

Under irradiation with a Xe lamp (300 W, >420 nm) equipped with a UV filter at room temperature in air, compounds **1–4** also exhibit excellent visible-light-induced photochromic behaviors (Fig. 5). As for **1** and **2**, coloration contrast is analogous to that of UV-light-induced photochromism but the photoresponsive rates and saturation time under visible light are significantly superior to those of UV-light. **1** and **2**

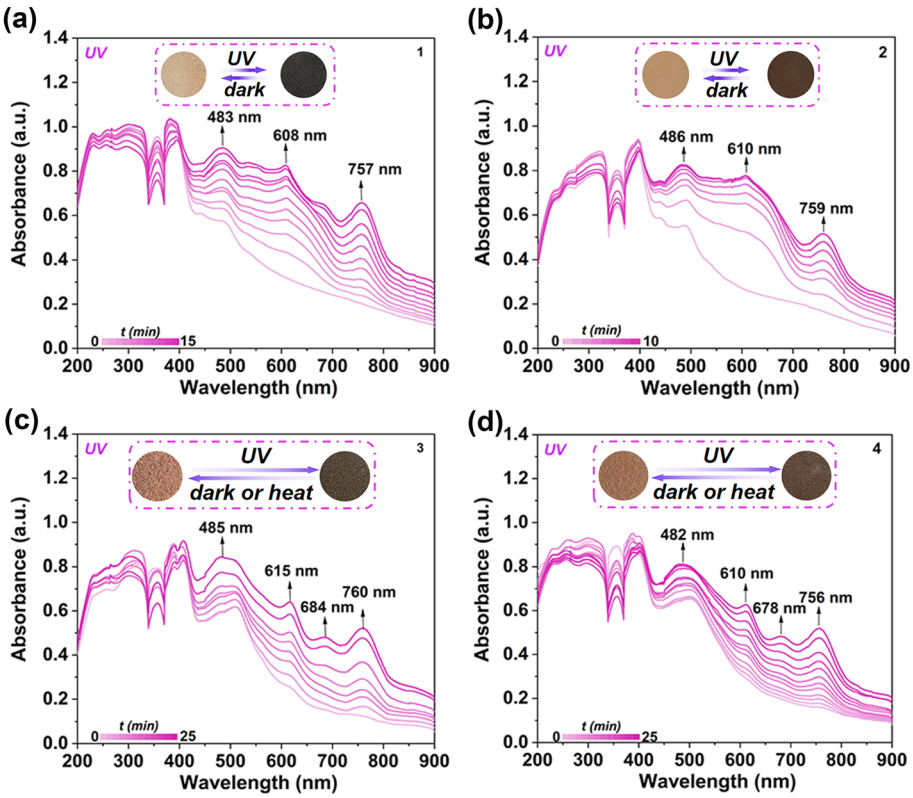

Fig. 4 Photochromic behaviors and time-dependent UV-vis absorption spectra of **1** (a), **2** (b), **3** (c) and **4** (d) upon 365 nm UV-light irradiation at room temperature (RT).

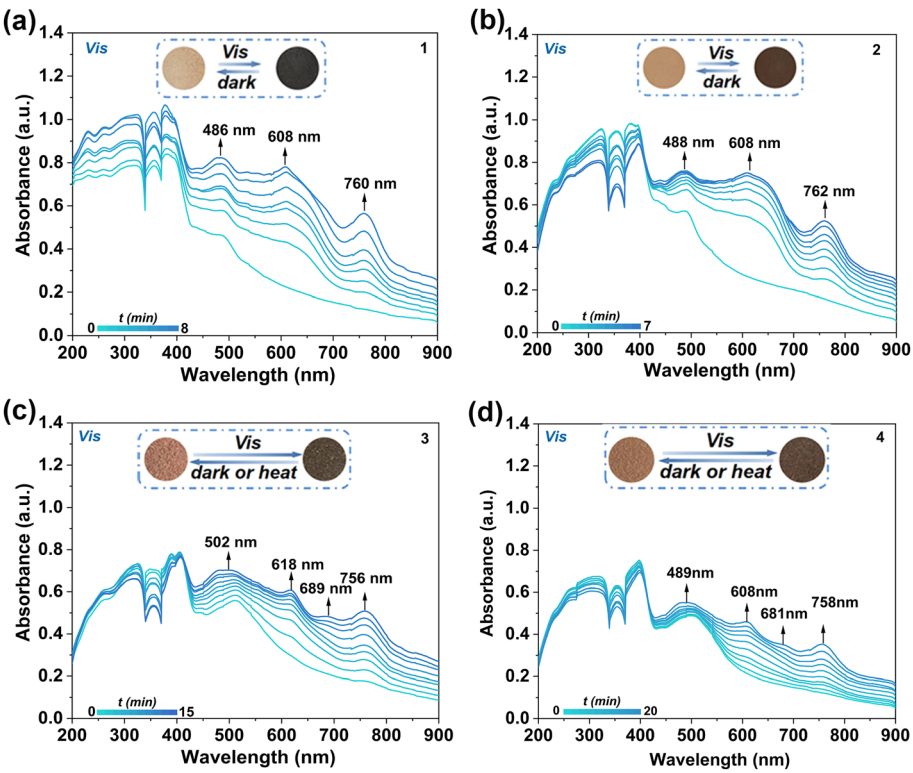

Fig. 5 Photochromic behaviors and time-dependent UV-vis absorption spectra of **1** (a), **2** (b), **3** (c) and **4** (d) upon visible-light (>420 nm) irradiation at RT.

begin to change color within 1 s and transition from their initial colors to the same saturated colors as **1P-UV** and **2P-UV** (denoted as **1P-Vis** and **2P-Vis**) with irradiation times of only 8 min and 7 min (Fig. 5a and b), respectively. Specifically, the ΔAbs values in 1 s upon visible-light irradiation are 0.21 for **1** and 0.28 for **2**, which are almost double with respect to the 0.11 and 0.14 obtained upon UV-light illumination (Fig. S5†). As for **3** and **4**, although the coloration contrast and the photoresponsive rates are basically comparable with those of UV-light illumination, the saturation time is shortened from 25 to 15 and 20 min (denoted as **3P-Vis** and **4P-Vis**), respectively. From the point of the change of absorption spectra, the ΔAbs values in 6 s (0.17) for **3** and 60 s (0.15) for **4** upon visible-light irradiation are primarily in agreement with that for UV light (0.15). In order to further ascertain the different photoresponsive rates of **1–4** under UV and visible light illumination, a more accurate method of kinetic evaluation was introduced to compare the photochromic rates of **1–4** based on the UV-vis absorption peaks at different irradiation times.

As shown in Fig. 6, the photochromic dynamics of **1–4** under visible-light (608 nm for **1**, **2** and **4**, and 618 nm for **3**) and UV-light irradiation (608 nm for **1**, 610 nm for **2** and **4**, and 615 nm for **3**) were also investigated using the following kinetics equation by selecting the UV-vis absorption peaks at different times: $\ln[(A_0 - A_\infty)/(A_t - A_\infty)] = k_t$, where A_0, A_t, and A_∞, respectively, are the absorption intensities at the onset of the photochromic behavior, the illumination duration, and the termination time, and k is the rate constant. The data should be divided into two portions and thereby could be well fit with a linearly increasing function with high R^2 values. Obviously, **1–4** display pseudo-first-order kinetics with two stages. As shown in Table S1,† the rate constants k for **1–4** in the first stage (denoted as k_1) are larger than those of the second stage (denoted as k_2). Specifically, in the first stage, the k values of visible-light photochromism are 0.161, 0.421, 6.5×10^{-2} and 2.4×10^{-2} s^{-1} for **1–4**, respectively, which are larger than those of UV-light photochromism (5.5×10^{-2}, 9.2×10^{-2}, 3.3×10^{-2} and 1.5×10^{-2} s^{-1} for **1–4**). In the second stages, the k values are dramatically reduced relative to those of the first stages, which can be ascribed to the photochromic behaviors concentrated on the crystal surface first and then in the inner cores. In other words, the efficiency of photon absorption from the surface to the interior gradually decreases. However, there is a consistent trend of faster visible-light responsive rates than those of UV-light (visible light: $k_2 = 1.8 \times 10^{-2}$, 4.0×10^{-2}, 3.2×10^{-3} and 2.5×10^{-3} s^{-1}, UV light: $k_2 = 5.0 \times 10^{-3}$, 1.3×10^{-2}, 2.8×10^{-3} and 2.1×10^{-3} s^{-1}). As shown in Fig. S7,† the order of the color change speeds for **1–4** is as follows: **2** > **1** > **3** > **4**, which is largely attributed to the different EA/ED interfacial contacts formed by the introduction of different positionally isomeric ligands and halogen anions.

Photochromic mechanism

To further verify the mechanism of photochromism, electron paramagnetic resonance (EPR) measurements were conducted at room temperature, in which **1**, **1P-Vis**, **2**, **2P-Vis**, **3**, **3P-UV**, **4**

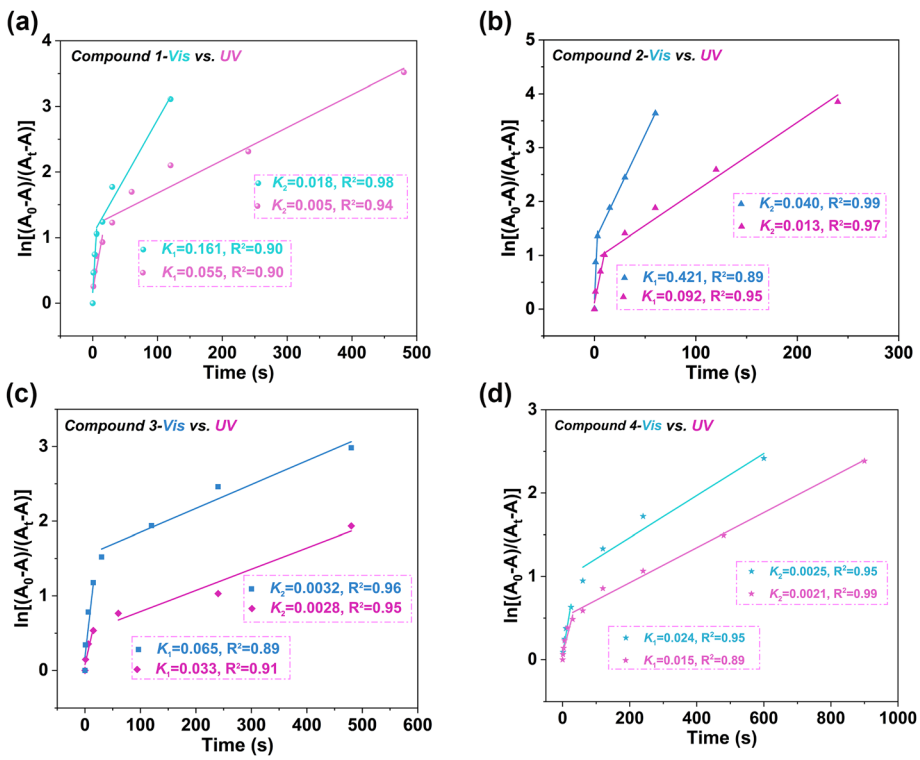

Fig. 6 Photochemical reaction kinetics comparison plots of **1** (a), **2** (b), **3** (c) and **4** (d) monitored at 608, 608, 618 and 608 nm upon visible-light (>420 nm) irradiation and at 608, 610, 615 and 610 nm upon UV-light (365 nm) illumination, respectively, under ambient conditions.

and **4P-UV** were selected as representatives (Fig. S8†). The results demonstrate that there are no obvious signals in the EPR spectra of compounds **1–4** before light illumination, but significantly enhanced sharp single-line EPR signals are observed. The *g* factors of 1.998 for **1P-Vis**, 2.000 for **2P-Vis**, 1.999 for **3P-UV** and 1.998 for **4P-UV** are close to the value of $[NDI]^{\bullet-}$ organic radicals (2.0023), further ascertaining that both UV-light and visible-light photochromic behaviors of **1–4** are caused by PIET. In addition, **1–4** display weak fluorescence. For instance, upon excitation at 365 nm, **3** and **4** exhibit emission bands centred at around 455 and 429 nm, respectively (Fig S13†). Meanwhile, the fluorescence emission intensities of **3P-UV** and **4P-UV** decrease dramatically (Fig S13†), which is attributed to the overlap of the fluorescence emission spectra and UV-vis absorption spectra, and consequently cause fluorescence quenching after coloration.[49]

In order to further understand the pathways of the generation of UV-light and visible-light induced radicals in detail, X-ray photoelectron spectroscopy (XPS) experiments were also performed (Fig. S9–S12†). As for **1** and **2**, the binding energies of N 1s shift to lower binding energies after visible-light irradiation (399.67 eV for **1** *vs.* 399.47 eV for **1P-Vis**, 400.32 eV for **2** *vs.* 400.20 eV for **2P-Vis**), implying that N atoms receive electrons as EAs from NDI cores. The binding energies of Cl 2p for **1** and Br 3d for **2** move toward higher binding energy positions after photostimulation (198.08 and 198.16 eV for **1** *vs.* 199.70 and 199.78 eV for **1P-Vis**, 68.87 and 69.83 eV for **2** *vs.* 68.97 and 69.93 eV for **2P-Vis**), implying that Cl and Br atoms lose electrons. The O 1s binding energies slightly shift toward higher binding energies for **1** and **2** after coloration (531.37 eV for **1** *vs.* 531.50 eV for **1P-Vis**, 531.67 eV for **2** *vs.* 531.88 eV for **2P-Vis**), which is probably ascribed to the delocalization effect of NDI cores after accepting electrons. As for **3** and **4**, the binding energies of N 1s also shift toward lower binding energies after UV-light illumination (400.16 eV for **3** *vs.* 400.04 eV for **3P-UV** and 400.20 eV for **4** *vs.* 400.06 eV for **4P-UV**). Differently, the core-level spectra of Cl 2p and Br 3d before and after irradiation are almost unchanged, implying that the Cl and Br atoms do not actually serve as EAs. Notably, the variations of overall signals of the O 1s binding energy are remarkable. In addition to the slight shift to higher binding energy positions (531.63 eV for **3** *vs.* 531.86 eV for **3P-UV** and 531.67 eV for **4** *vs.* 531.88 eV for **4P-UV**), new prominent peaks centred at 532.97 eV for **3P-UV** and 533.02 eV for **4P-UV** are observed, indicating that the O atoms lose electrons. Therefore, electrons are transferred from electron-rich halogen atoms to the electron-deficient NDI nucleus in **1** and **2**, while PIET occurs between electron-rich O atoms and electron-deficient NDI cores in **3** and **4**. The different pathways of the formation of $[3\text{-PMNDI}]^{\bullet-}$/$[4\text{-PMNDI}]^{\bullet-}$ should be attributed to the concurrence of distinct interfacial contacts of EDs/EAs as discussed in detail below.

Besides the electron donating/accepting abilities of EDs/EAs, the interfacial contact of EDs/EAs is one of the most important factors for determining the photochromic properties of CPs based on PIET. As shown in Fig. 7, the use of positionally isomeric ligands (4-/3-PMNDI) leads to specific interfacial contacts, which further result in CT interactions and concomitantly the generation of non-characteristic absorption bands in the visible-light region. The special CT interactions can be applied to stimulate PIET from the HOMO of EDs to the LUMO of EAs and consequently generate the organic radicals of $[PMNDI]^{\bullet-}$, causing the visible-light photochromic properties of **1–4**. The higher photosensitivity of **1–4** in response to visible-light than that to UV-light is attributed to the higher excitation efficiency of the electronic absorption band of CT interactions (visible-light region) than that of the characteristic absorption of EAs (UV-light region). Furthermore, the discriminative photoresponsive rates of **1–2** and **3–4** could be contributed to two different types of interfacial contacts of discrete [ED–EA–ED] in **1** and **2** and infinite [–ED–EA–ED–] in **3** and **4** through the different types and strengths of weak interactions (anion–π interactions: 3.319(4) Å for **1** and 3.332(8) Å for **2**; lone pair–π interactions: 3.606(3) Å for **3** and 3.719(3) Å for **4**; π–π interactions: 3.822(3) Å for **3** and 3.929(3) Å for **4**) (Fig. 7). Furthermore, the faster photoresponsive rate of **2** than that of **1** could be attributed to the introduction of different halogens, in which bromine atoms possess lower electronegativity but have a larger atomic radius than chlorine atoms, indicating that bromine atoms are more likely to donate electrons than chlorine. The superior photochromic performance of **3** relative to that of **4** is mainly attributed to stronger n–π and π–π interactions.

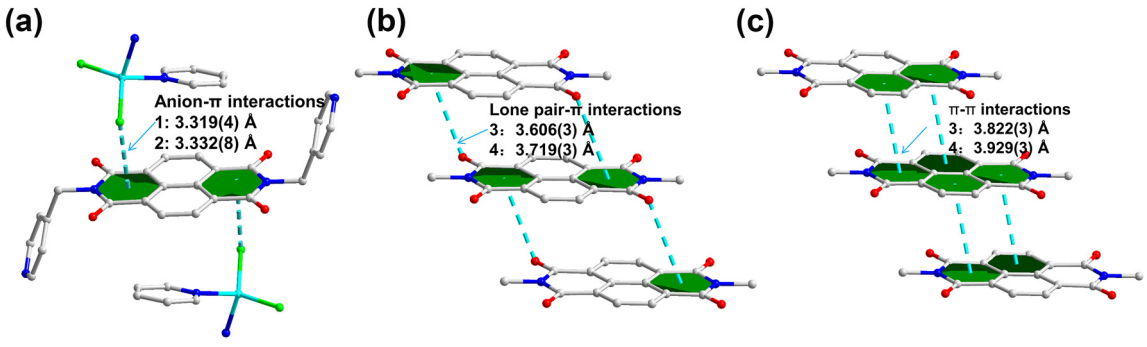

Fig. 7 (a) Interfacial contacts for **1** and **2** and (b and c) for **3** and **4**. All hydrogen atoms are omitted for clarity.

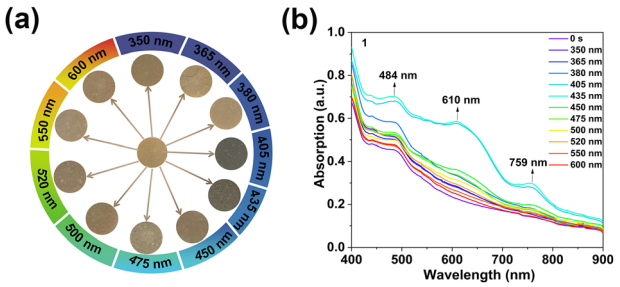

Fig. 8 (a) Photochromic behaviors and (b) the UV-vis absorption spectra of **1** under excitation of visible light with different wavelengths.

Visual detection and filtration of harmful blue rays

In recent years, the influence of blue light on human health has received significant public concern due to the widespread use of electronic devices such as televisions, laptops, tablets and smartphones.[50] Blue light can be more precisely classified into two categories: "high-energy visible blue-violet light" (400–450 nm) and "circadian rhythm blue-turquoise light" (460–470 nm).[51] The former can result in retinal injury caused by photochemical damage, while the latter has been shown to modulate circadian rhythm activity as assessed through melatonin suppression. Therefore, there is an imperative need to develop optical functional materials with a simple and intuitive approach for detecting (absorbing) harmful blue rays, with the objective of reducing harm to human eyesight and sleep.

Owing to the excellent photoresponsive rate to the visible-light source, the potential of compound **1** for practial application was assessed in detecting and filtering harmful blue light. The photochromic behaviors of **1** were carefully investigated under the irradiation of light with different wavelengths (350, 365, 380, 405, 435, 450, 475, 500, 520, 550 and 600 ± 15 nm) for 60 s. As depicted in Fig. 8a, **1** is highly sensitive to visible light in the range of 390–450 nm with a significant visual change from yellow to greyish-green. Meanwhile, the characteristic absorption bands of $[PMNDI]^{\bullet-}$ centered at 484, 610 and 759 nm in the range of 400–900 nm were observed in the UV-vis absorption spectra after light illumination (Fig. 8b), which is similar to that of **1P-Vis**, indicating the formation of the PIET process. The typical sensitivity range at light wavelengths of 390–450 nm is in good agreement with the wavelength range of harmful blue rays (400–450 nm). Therefore, compound **1** is shown to be one of the candidate materials for the visual detection/filtration of harmful blue rays through its distinct photochromic behavior, and it can also be applied for the construction of a harmful-blue light filter.

Conclusions

In summary, four visible-light photosensitive coordination polymers were successfully constructed by the combination of electron-deficient 4-/3-PMNDI positional isomers and electron-rich zinc halides. Strikingly, the photoresponsive rates of visible-light photochromism for **1–4** are much faster than those of UV-light photochromism. This demonstrates that the electronic absorption bands of the CT interactions in the visible-light region can efficiently induce ET quickly. Furthermore, **1** is highly sensitive to harmful blue light in the range of 390–450 nm, which can be used for accurately detecting or filtering harmful blue rays. This work developed a novel photoexcitation mechanism for initiating the ET process, providing a straightforward and efficient pathway for the construction of visible-light photochromic materials for detecting/filtering harmful blue rays.

Author contributions

Xiaojuan Zhang: conceptualization, investigation, analyzing the data, and writing the original draft; Ming Kang: carrying out the experiments and performing most of the tests; Shiming Zhang: crystal structure solving and refinement and data curation; Jingfang Wang: modifying the experiments and visualization; Yifang Zhang: helping to write the original draft and visualization; Junju Shen: conceptualization and supervision; Pengfei Hao: writing (review and editing), supervision, methodology and funding acquisition; Yunlong Fu: conceptualization, writing (review and editing), and supervision.

Conflicts of interest

There are no conflicts to declare.

Data availability

All relevant data are within the manuscript and its ESI.†

Acknowledgements

This work was supported by the National Natural Science Foundation of China (21171110), the Natural Science Foundation of Science and Technology Agency of Shanxi Province (20210302123324, 201901D111275), the Graduate Education Innovation Project of Shanxi Province (2024XBY05), and the 1331 Project of Shanxi Province.

References

1 D. Bléger and S. Hecht, Visible–light–activated molecular switches, *Angew. Chem., Int. Ed.*, 2015, **54**, 11338–11349.
2 J. R. Hemmer, S. O. Poelma, N. Treat, Z. A. Page, N. D. Dolinski, Y. J. Diaz, W. Tomlinson, K. D. Clark, J. P. Hooper, C. Hawker and J. Read de Alaniz, Tunable visible and near infrared photoswitches, *J. Am. Chem. Soc.*, 2016, **138**, 13960–13966.
3 K. Hüll, J. Morstein and D. Trauner, In vivo photopharmacology, *Chem. Rev.*, 2018, **118**, 10710–10747.

4 Z. W. Zhang, W. H. Wang, M. O'Hagan, J. H. Dai, J. J. Zhang and H. Tian, Stepping out of the blue: from visible to near–IR triggered photoswitches, *Angew. Chem., Int. Ed.*, 2022, **61**, e202205758.
5 H. B. Cheng, S. C. Zhang, E. Y. Bai, X. Q. Cao, J. Q. Wang, J. Qi, J. Liu, J. Zhao, L. Q. Zhang and J. Y. Yoon, Future-oriented advanced diarylethene photoswitches: from molecular design to spontaneous assembly systems, *Adv. Mater.*, 2022, **34**, 2108289.
6 R. J. Li, T. Ou, L. Wen, Y. H. Yan, W. Li, X. L. Qin and S. X. Wang, All-visible-light-activated diarylethene photoswitches, *Molecules*, 2024, **29**, 5202.
7 R. Siewertsen, H. Neumann, B. Buchheim-Stehn, R. Herges, C. Näther, F. Renth and F. Temps, Highly efficient reversible *Z–E* photoisomerization of a bridged azobenzene with visible light through resolved $S_1(n\pi^*)$ absorption bands, *J. Am. Chem. Soc.*, 2009, **131**, 15594–15595.
8 E. Titov, Visible light induced exciton dynamics and *trans*-to-*cis* isomerization in azobenzene aggregates: insights from surface hopping/semiempirical configuration interaction molecular dynamics simulations, *ACS Omega*, 2024, **9**, 8520–8532.
9 C. H. Wu, P. Q. Nhien, T. T. K. Cuc, B. T. B. Hue and H. C. Lin, Designs and applications of multi-stimuli responsive FRET processes in aIEgen-functionalized and bi-fluorophoric supramolecular materials, *Top. Curr. Chem.*, 2023, **381**, 388.
10 Z. Y. Bai, L. Guo, D. Zhao and Y. G. Wang, Photochromic spiropyran-based dual-emitting luminescent hybrid films for dynamic information anticounterfeiting, *ACS Appl. Mater. Interfaces*, 2024, **16**, 44018–44025.
11 M. M. Lerch, W. Szymański and B. L. Feringa, The (photo) chemistry of Stenhouse photoswitches: guiding principles and system design, *Chem. Soc. Rev.*, 2018, **47**, 1910–1937.
12 C. A. Reyes, H. J. Lee, C. Karanovic and E. Picazo, Development and characterization of amino donor-acceptor Stenhouse adducts, *Nat. Commun.*, 2024, **15**, 5533.
13 P.-Y. Guo, C. Sun, N.-N. Zhang, L.-Z. Cai, M.-S. Wang and G.-C. Guo, An inorganic–organic hybrid photochromic material with fast response to hard and soft X-rays at room temperature, *Chem. Commun.*, 2018, **54**, 4525–4528.
14 S.-D. Han, J.-X. Hu and G.-M. Wang, Recent advances in crystalline hybrid photochromic materials driven by electron transfer, *Coord. Chem. Rev.*, 2022, **452**, 214304.
15 J.-L. Zhao, M.-H. Li, Y.-M. Cheng, X.-W. Zhao, Y. Xu, Z.-Y. Cao, M.-H. You and M.-J. Lin, Photochromic crystalline hybrid materials with switchable properties: Recent advances and potential applications, *Coord. Chem. Rev.*, 2023, **475**, 214918.
16 X. Y. Ren, F. Y. Chen, C. H. Zhang, Z. G. Liang, X. Y. Yu, S. D. Han and G. M. Wang, Regulating the topologies and photoresponsive properties of lanthanum-organic frameworks, *Chem. – Eur. J.*, 2024, **30**, e202402581.
17 Y. Chen, A.-G. Liu, Z.-T. Chen, X.-H. Liang, J.-T. Yan and B. Li, Efficient IrIII Photosensitizer Incorporated in the Metal–Organic Framework with the Bis-lophine-bipyridine Motif for $C(sp^3)$-C/N–H Cross-Coupling Reactions, *ACS Catal.*, 2024, **14**, 16605–16617.
18 O. A. Stasyuk, A. A. Voityuk, A. J. Stasyuk and M. Solà, Photoinduced electron transfer in inclusion complexes of carbon nanohoops, *Acc. Chem. Res.*, 2023, **57**, 37–46.
19 J. Q. Pan, H. R. Wei, Y. R. Chen, M. Z. Jia, B. Tan and J. Zhang, Photomodulation of charge transfer through excited–state processes: directing donor–acceptor binding dynamics, *Angew. Chem., Int. Ed.*, 2024, **64**, e202412790.
20 Z. Xu, A. Chandresh, A. Mauri, M. Esmaeilpour, V. Monnier, F. Odobel, L. Heinke, W. Wenzel, M. Kozlowska, S. Diring, R. Haldar and C. Wöll, Regulated charge transfer in donor-acceptor metal–organic frameworks for highly-sensitive photodetectors, *Angew. Chem., Int. Ed.*, 2024, **63**, e202414526.
21 M. U. Rahman, Y. F. Yuan, J. L. Yan, Y. Q. Xu, Z. Y. Cao, Y. Xu, J. X. Liu and M. H. Li, Series of viologen-based metal-oxalate frameworks showing ultrafast-response photo/electrochromic and UV detection behavior, *J. Alloys Compd.*, 2025, **1013**, 178621.
22 L. Li, S. H. Li, Z. Y. Li, N. N. Zhang, Y. T. Yu, J. G. Zeng and Y. Hua, Advances in viologen-based stimulus-responsive crystalline hybrid materials, *Coord. Chem. Rev.*, 2024, **518**, 216064.
23 Z. F. Liu, X. B. Li, W. J. Dai, J. J. Liu and M. J. Lin, Naphthalenediimide and perylenediimide based donor-acceptor crystalline hybrid materials: structures and applications, *Coord. Chem. Rev.*, 2025, **526**, 216350.
24 L. Li, J.-G. Zeng, N.-N. Zhang, Y.-T. Yu, S.-H. Li and Y. Hua, Naphthalene diimide-based crystalline hybrid photochromic materials: structural types, photochromic mechanism, and applications, *Inorg. Chem. Front.*, 2025, **12**, 11–38.
25 Y. J. Ma, S. D. Han, J. Pan, Y. Mu, J. H. Li and G. M. Wang, An inorganic-organic hybrid framework from the assembly of an electron-rich diphosphonate and electron-deficient tripyridyl moiety, *J. Mater. Chem. C*, 2018, **6**, 9341–9344.
26 J. Li, Y. H. Wang, S. D. Han, Y. X. Wen, J. X. Hu, J. H. Li and G. Y. Yang, Photochromism and photomagnetism in Two Ni(II) complexes based on a photoactive 2,4,6-tris-2-pyridyl-1,3,5-triazine ligand, *Inorg. Chem.*, 2024, **63**, 1142–1150.
27 H. Javed, K. Fatima, Z. Akhter, M. A. Nadeem, M. Siddiq and A. Iqbal, Fluorescence modulation of cadmium sulfide quantum dots by azobenzene photochromic switches, *P. Roy. Soc. A*, 2016, **472**, 20150692.
28 Y.-C. Chen, Y.-M. Di, S.-Q. Zhang and M.-J. Lin, Polyoxometalate/s-triazine hybrid heterostructures with ultrafast photochromic properties, *Dalton Trans.*, 2024, **53**, 3215–3223.
29 L. Li, Y.-T. Yu, N.-N. Zhang, S.-H. Li, J.-G. Zeng, Y. Hua and H. Zhang, Polyoxometalate (POM)-based crystalline hybrid photochromic materials, *Coord. Chem. Rev.*, 2024, **500**, 215526.
30 B. Q. Zhong, J. L. Liu, G. C. Liu, Z. Zhang, Y. Q. Chen and X. L. Wang, , pH-directed polyoxometalate-based supramo-

lecular framework for effectively electrochemical sensing IO_3^- from glycerol oxidation wastewater, *J. Mol. Struct.*, 2025, **1332**, 141679.

31 J. J. Shen, X. l. Kang, P. F. Hao and Y. L. Fu, Semiconductive donor promoted photochromism of iodoplumbate hybrids, *Inorg. Chem. Front.*, 2020, **7**, 4865–4871.

32 P. F. Hao, B. H. Gao, G. P. Li, J. J. Shen and Y. L. Fu, Ultrafast visible-light photochromic properties of naphthalenediimide-based coordination polymers for the visual detection/filtration of blue light, *Inorg. Chem. Front.*, 2022, **9**, 2852–2861.

33 S. M. Zhang, P. F. Hao, G. P. Li, J. J. Shen and Y. L. Fu, Multifunctional naphthalene diimide-based coordination polymers: ultrafast visible light-induced photochromism, visual detection of blue light, inkless and erasable prints and electrochromism, *Dyes Pigm.*, 2023, **220**, 111677.

34 S. M. Zhang, P. F. Hao, Y. F. Zhang, G. P. Li, J. J. Shen, H. Y. Yang and Y. L. Fu, Mechanism of the generation of ultra-stable radicals in fast photochromic naphthalenediimide-based coordination polymers, *Inorg. Chem. Front.*, 2025, **12**, 3919–3926.

35 Y.-S. Shi, D.-D. Yang, T. Xiao, Z.-G. Xia, Y.-H. Fang and X.-J. Zheng, Photoinduced multi-color emission of naphthalenediimide radical in different solvents and dynamic anti-counterfeiting film, *Chem. Eng. J.*, 2023, **472**, 145152.

36 J. Z. Liao, Y. Jiang, F. F. He, L. L. Jiang, X. M. Zhu and H. Ke, Photo-induced organic radical species in naphthalenediimide-based metal-organic framework for reversible photochromism and near-infrared photothermal conversion, *Mater. Today Chem.*, 2023, **27**, 101324.

37 S. M. Zhang, P. F. Hao, Y. F. Zhang, G. P. Li, J. J. Shen and Y. L. Fu, The simultaneous modulation effect of N-substituents on the photochromic and electrochromic properties of naphthalenediimide-based coordination polymers, *Inorg. Chem. Front.*, 2024, **11**, 1226–1237.

38 J. B. Dai, Y. F. Zu, Y. Yang, C. Y. Yang, Y. Yu, S. Q. Zhang and J. H. Hou, Thermal cross-linking preparation of aqueous-based cathodic films for enhanced stability in organic electrochromic devices, *Chem. Eng. J.*, 2024, **487**, 150473.

39 H.-Y. Deng, J.-R. He, M. Pan, L. Li and C.-Y. Su, Synergistic metal and anion effects on the formation of coordination assemblies from a *N*,*N*′-bis(3-pyridylmethyl)naphthalene diimide ligand, *CrystEngComm*, 2009, **11**, 909–917.

40 O. V. Dolomanov, L. J. Bourhis, R. J. Gildea, J. A. K. Howard and H. Puschmann, OLEX2: a complete structure solution, refinement and analysis program, *J. Appl. Crystallogr.*, 2009, **42**, 339–341.

41 G. Sheldrick, A short history of SHELX, *Acta Crystallogr., Sect. A*, 2008, **64**, 112–122.

42 G.-B. Li, J.-R. He, J.-M. Liu and C.-Y. Su, Anion effect on the structural diversity of three 1D coordination polymers based on a pyridyl diimide ligand, *CrystEngComm*, 2012, **14**, 2152.

43 L. Yang, D. R. Powell and R. P. Houser, Structural variation in copper(I) complexes with pyridylmethylamide ligands: structural analysis with a new four-coordinate geometry index, τ_4, *Dalton Trans.*, 2007, **9**, 955–964.

44 J.-J. Liu, S.-B. Xia, D. Liu, J.-Y. Hou, H.-B. Suo and F.-X. Cheng, Multifunctional naphthalene diimide-based coordination polymers: Photochromism and solventchromism, *Dyes Pigm.*, 2020, **177**, 108269.

45 J.-J. Liu, Y.-F. Guan, Y. Chen, M.-J. Lin, C.-C. Huang and W.-X. Dai, The impact of lone pair–π interactions on photochromic properties in 1-D naphthalene diimide coordination networks, *Dalton Trans.*, 2015, **44**, 17312–17317.

46 S. Guha, F. S. Goodson, S. Roy, L. J. Corson, C. A. Gravenmier and S. Saha, Electronically regulated thermally and light-gated electron transfer from anions to naphthalenediimides, *J. Am. Chem. Soc.*, 2011, **133**, 15256–15259.

47 S. Guha, F. S. Goodson, L. J. Corson and S. Saha, Boundaries of anion/naphthalenediimide interactions: from anion–π interactions to anion-induced charge-transfer and electron-transfer phenomena, *J. Am. Chem. Soc.*, 2012, **134**, 13679–13691.

48 M. Kang, B. H. Gao, S. M. Zhang, P. F. Hao, G. P. Li, J. J. Shen and Y. L. Fu, The effect of conjugation degree of aromatic carboxylic acids on electronic and photo-responsive behaviors of naphthalenediimide-based coordination polymers, *Dalton Trans.*, 2023, **52**, 12030–12037.

49 P. F. Hao, W. P. Wang, J. J. Shen and Y. L. Fu, Photochromic and luminescent switchable iodoargentate hybrids directed by solvated lanthanide cations, *Dalton Trans.*, 2020, **49**, 8883–8890.

50 H. Chakravarthy, V. Georgyev, C. Wagen, A. Hosseini and J. Matsubara, Blue light-induced phototoxicity in retinal cells: implications in age-related macular degeneration, *Front. Aging Neurosci.*, 2024, **16**, 1509434.

51 S. A. Giannos, E. R. Kraft, L. J. Lyons and P. K. Gupta, Spectral evaluation of eyeglass blocking efficiency of ultraviolet/high-energy visible blue light for ocular protection, *Optom. Vis. Sci.*, 2019, **96**, 513–522.